# The Role of OOH Binding Site and Pt Surface Structure on ORR Activities

**Qingying Jia**[a], **Keegan Caldwell**[b], **Joseph M. Ziegelbauer**[c,*], **Anusorn Kongkanand**[c], **Frederick T. Wagner**[c,*], **Sanjeev Mukerjee**[a,**], and **David E. Ramaker**[b,z,*]

[a]Department of Chemistry & Chemical Biology, Northeastern University, Boston, Massachusetts 02115, USA

[b]Department of Chemistry, George Washington University, Washington, DC 20052, USA

[c]Electrochemical Energy Research Lab, General Motors Research & Development, Warren, Michigan 48090, USA

## Abstract

We present experimentally observed molecular adsorbate coverages (e.g., O(H), OOH and HOOH) on real operating dealloyed bimetallic $PtM_x$ (M = Ni or Co) catalysts under oxygen reduction reaction (ORR) conditions obtained using X-ray absorption near edge spectroscopy (XANES). The results reveal a complex Sabatier catalysis behavior and indicate the active ORR mechanism changes with Pt–O bond weakening from the $O_2$ dissociative mechanism, to the peroxyl mechanism, and finally to the hydrogen peroxide mechanism. An important rearrangement of the OOH binding site, an intermediate in the ORR, enables facile H addition to OOH and faster O–O bond breaking on 111 faces at optimal Pt–O bonding strength, such as that occurring in dealloyed PtM core-shell nanoparticles. This rearrangement is identified by previous DFT calculations and confirmed from in situ measured OOH adsorption coverages during the ORR. The importance of surface structural effects and 111 ordered faces is confirmed by the higher specific ORR rates on solid core vs porous multi-core nanoparticles.

In recent years it has been well-established that PtM (M = Co, Ni, Cu) core-shell nanoparticles (NPs) are 5–15 times more reactive for the oxygen reduction reaction (ORR) than pure Pt NPs of comparable size.[1–5] These core-shell NPs are produced most easily by (electro)chemically dealloying PtM NPs in acid, with the more active M metal leaching out faster allowing formation of the Pt skin. Experimentally and theoretically it has been established that lattice compression of the outer Pt skin covering the PtM rich core is the primary reason for the enhanced ORR activity, as this lattice compression causes a widening and negative shift of the Pt d-band.[1,6] This weakens the Pt–O bond (the important ORR catalyst's "descriptor")[7,8] and therefore the bonding also of other key intermediates (e.g.

[*]Electrochemical Society Active Member.

[**]Electrochemical Society Fellow.

[z]ramaker@gwu.edu

OH, OOH, HOOH), because these all involve bonding through the O atom.[9] Finally the ORR rate has been found to change very uniformly and systematically with M content consistent with Vegards law;[10,11] the more M atoms in the core the more lattice compression of the skin.[1]

Despite these well-established correlations, it has not been experimentally verified just how the three previously proposed ORR mechanisms change. These mechanisms are differentiated primarily by indicating the molecular species when the di-oxygen bond breaks, namely as $O_2$, OOH, or HOOH; the addition of H weakening the di-oxygen bond and therefore making bond breaking easier. How do these rates change with Pt–O bond weakening and hence what intermediates dominate the adsorbate coverage on the Pt surface?

In this work we report direct measurement of the OH, OOH and HOOH intermediate coverage, using in situ X-ray absorption spectroscopy (XAS) during the ORR and show that all three mechanisms play a dominant role at some point with Pt–O bonding weakening (i.e. M/Pt ratio)and that the total yield consists of the sum of all three processes.[12] We further show that surface effects (Pt structural order) also play a role even on 5–7 nm PtM core-shell NPs. It has been shown previously that on much larger Pt polycrystals surface roughness and order played a role,[13] and of course the ORR rate has been shown to be significantly different on the 100, 110 and 111 SC planar surfaces.[14,15] Particles size effects have also been shown to play a role because the fraction of ordered 100 and 111 planes vs. corners and edges change with size,[16–18] but we use similar sized NPs here, and show that the porosity of the Pt core and skin play a more significant role.

The results are obtained by studying 16 different catalysts, as summarized in Table I, with varying M (M = Co and Ni)/Pt ratio and Pt skin porosity, using XAS data to show how core and skin porosity alter the intermediate OOH coverage and the dominant ORR mechanism. The skin porosity has been changed using alternate gas environments and acids as indicated in Table I to vary the M leaching process rate and thereby the porosity of the NP as discussed elsewhere.[19]

## ORR kinetics and possible intermediate adsorbate coverage

One might ask, what adsorbate intermediates are even expected on the surface during the ORR? Understanding the ORR intermediate species, such as O, OH, OOH, and coverage on catalyst surfaces is critical for understanding the fundamental kinetic mechanisms in a fuel cell.
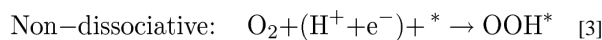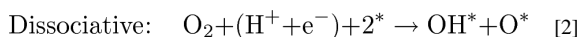
The ORR kinetics has been well modeled with the rate expression[13,20,21]

$$i = nF\,k\,c_{O_2}\exp(-\alpha FV/RT)\exp(-\Delta G_{rds}/RT)\,(1-\theta_{tad}), \quad [1]$$

where $RT/\alpha F$ is the Tafel slope, and the factors out front are the number, n, of electrons transferred (one) in the rate determining step (RDS), the oxygen concentration, $c_{O2}$, and the exchange rate constant, k, of the rds. Here, V is the overpotential, and the important
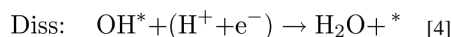
parameters for this discussion are $\theta_{tad}$ and $\Delta G_{rds}$. $\theta_{tad}$ is the total adsorbate (tad) coverage of all intermediates and other anions and $\Delta G_{rds}$ is the activation energy of the rds. The possible intermediates on the surface can be any or all of the following: O, $O_2$, OH, OOH, $H_2O_2$, and $H_2O$ and nearly all of these have been somehow associated with the rds in previous reports far too numerous to review here.

To simplify matters, we follow Koper[8] who separated the obstacles to an overall reaction into the "kinetic bottleneck" (the rds) vs the "thermodynamic bottleneck", the latter the primary adsorbate determining step, or more often called[22–24] the potential determining step (pds). The ORR rds apparently involves getting the initial adsorbate on the surface in either of two mechanisms:

$$\text{Dissociative:}\quad O_2+(H^++e^-)+2^* \rightarrow OH^*+O^* \quad [2]$$

$$\text{Non-dissociative:}\quad O_2+(H^++e^-)+^* \rightarrow OOH^* \quad [3]$$

The fact that eq. 1 models the kinetics, with the proper dependency on $c_{O2}$, pH, n, and V (Tafel slope), points to the reactants on the left side of 2) or 3) being involved in the rds. Further the constant activation energy ($\Delta G_{rds} = 40$ kJ/mol) determined from Arrhenius plots for Pt and Pt-M catalysts,[25] points to the rds involving perhaps some weakly bonded intermediate, perhaps physisorbed $O_2$ or even $O_2$ in the inner Helmholtz layer. This is because a more tightly bonded intermediate on the surface, such as $OH^*$ or $OOH^*$ would change $\Delta G_{rds}$ with Pt–O bond strength (i.e. changed Pt surface), assuming a linear Bronsted, Evans, Polanyi (BEP) relation between the activation energy and reactive intermediate free energy, $\Delta G_{ri}$; i.e. if $\Delta G_{rds} = \gamma \Delta G_{ri}$ where $\gamma$ is the BEP constant and $\Delta G_{ri}$ should track with the Pt–O binding energy as noted above.[8,26]

The primary adsorbate making up the $\theta_{tad}$ will be determined by the pds, which is the most unfavorable step thermodynamically on the surface, or often the last step to become downhill in free energy with increasing potential.[22–24] That step is the "thermodynamic bottleneck" on the surface and therefore determines the primary adsorbate on the surface and also the magnitude of $\theta_{tad}$, not necessarily the rds. This pds has been proposed as one of the reactions:[27–30]

$$\text{Diss:}\quad OH^*+(H^++e^-) \rightarrow H_2O+^* \quad [4]$$

$$\text{Non-Diss, } OOH^*:\quad OOH^*+^* \rightarrow O+OH^* \quad [5]$$

$$\text{Non-Diss, } HOOH^*:\quad HOOH^*+^* \rightarrow 2OH^*; \quad [6]$$

leading to the dissociative, peroxyl, or hydrogen peroxide mechanisms respectively. Here the $^*$ indicates an empty Pt site, and the $ad^*$ indicates an adsorbate on a Pt site. In the dissociative mechanism,[27–30] as the name implies, the Pt–$O_2$ bond is so strong that the

bonding involves electron transfer from Pt to the $O_2$ and therefore simultaneous breaking of the $O_2$ bond as in (2). The $OOH^*$ and $HOOH^*$ mechanisms imply a weaker non-dissociative Pt–$O_2$ bond, and therefore 1 or 2 ($H^+ + e^-$) additions are needed to help break the $O_2$ bond. Thus the nature of the slow step on the surface, the pds, is very much determined by the nature of the Pt catalysts (particle size, shape and microstructure), because the pds is determined by the strength of the Pt–O bond involving the ORR intermediates adsorbed on the surface (and as noted above also by the potential). The pds primarily determines the ORR rate through the $\theta_{tad}$.

## Previous attempts at in situ adsorbate measurements

Unfortunately, obtaining complete clarity on the ORR mechanism requires measurement of the adsorbed reaction intermediates, and this has proven to be very challenging, particularly on real operating electrocatalysts. Experimental verification of the Sabatier principle, i.e. observation of $OOH_n^*$ on the Pt–O weak side and $O(H)^*$ on the strong side of the volcano plot, has been elusive (we use $OOH_n$ as short hand for OOH or HOOH and O(H) for O or OH).

**T**his work is not the first attempt at obtaining in situ adsorbate coverages during the ORR. We briefly summarize four previously reported in situ adsorbate measurements, which attempted to follow the adsorbates on a Pt cathode in situ with potential.

1.  Using ATR-FTIR (attenuated total reflectance-Fourier transform infrared) spectroscopy, Kunimatsu et al.[31] examined adsorbates during the ORR on a thick Pt polycrystalline film (100 nm particles) in acid. These measurements were preceded by similar measurements in alkaline for a Pt film.[32,33] Both of these measurements were able to follow an FTIR peak attributed to the O–O stretch of either the superoxide anion, $O_2^-$ or $O_2(ads)$ on the surface. They proposed an end-on, somewhat tilted orientation of the $O_2^*$, as some component perpendicular to the surface is required in order for it to be IR active. The $O_2^*$ coverage (absent in $N_2$ sparged electrolyte) peaked around 0.75 V vs. RHE when moving cathodically, and Kunimatsu et al.[31] therefore suggested that this was $O_2^*$ preceding the dissociation step, which is in pre-equilibrium with the rds, $O^* + (H^+ + e^-) \rightarrow OH^*$.

2.  Using in situ XANES (x-ray absorption near edge spectroscopy), Erickson et al.[34] examined the ORR on ~3 nm Pt/C, with high $O_2$ flux. The increased XANES near edge intensity or "whiteline" (i.e. $\Delta W = W(V) - W(0.4\ V)$) was used to track Pt oxidation. The increased $\Delta W$ in the presence of $O_2$ vs $N_2$ sparged electrolyte was attributed either to increased $OH^*$ or $O_2^*$ on the surface, i.e. the $\Delta W$ increases for both and thus these could not be distinguished.

3.  Using EC-XPS (X-ray photoelectron spectroscopy combined with an electrochemical cell), Watanabe et al.[25] followed the adsorbates on polycrystalline Pt and PtM (M = Fe, Co, and Ni) bimetallics having a Pt skin. The Pt $4f_{7/2}$ peak was deconvoluted into contributions attributed to adsorbed $H_2O^*$, $OH^*$, and $O^*$. They attributed the higher ORR activity of the PtM to the increased $O^*$ coverage observed in this case, and therefore indicated the rds is $O^* + (H^+ + e^-) \rightarrow OH^*$.

4. More recently using APXPS (ambient pressure XPS), Casalongue et al.[35] deconvolved the XPS O 1s peak obtained from an operating fuel cell Pt cathode into 6 different contributions ($H_2O_{ml}$, $H_2O_{ad}$, $OH–H_2O$, $H_2O–\underline{OH}$, $\underline{OH}–O$, $OH–\underline{O}$ with the underlined atom bound to the Pt) involving $H_2O$, hydrated and non-hydrated OH and O with OH. Unfortunately the deconvolution into so many contributing species is not unique as acknowledged by the authors, but they were able to detect the changing coverage of hydrated and nonhydrated OH with potential and $O_2$ pressure. These results suggested that under normal hydrated conditions, the pds is $OH_{ad}$ leaving the surface of Pt.

These experimental studies can be summarized as follows: except in the ATR-FTIR experiment, where only $O_2^*$ was followed, it was difficult if not impossible to distinguish mono- from di-oxygen species, $OH^*$ from $OOH_n^*$, and in all cases the dissociative mechanism was suggested with $O^*$ or $OH^*$ as the intermediate in the pds. Thus these experiments never confirmed the Sabatier principle because they could not simultaneously track $OOH_n^*$ vs. $OH^*$ or distinguish them clearly from $O_2^*$.

## Experimental

### Catalyst preparation

The dealloyed $PtNi_3/C$ catalysts were produced via a three step process: 1) the precursor was prepared by an impregnation method, 2) followed by a high temperature annealing step, and 3) chemically dealloyed by acid leaching as described more fully elsewhere.[5] The final catalyst powder was then manually ground in an agate mortar and pestle prior to preparing the MEA inks.

We report, as summarized in Table I, results for various dealloyed $PtM_3/C$ (M = Co and Ni) catalysts at 3 different stages of life (after 200 (beginning of life -BOL), 10 k and 30 k (end of life - EOL) cycles giving 16 different PtM catalysts plus pure Pt). These 16 catalysts were demonstrated in fuel cell testing to give excellent oxygen reduction activity and durability, exceeding DOE 2017 targets.[36] The development of these highly active catalysts and further characterization will be reported elsewhere.[37] The catalysts are differentiated by the acid used for leaching the M atom ($HNO_3$ or $H_2SO_4$ denoted NA or SA) and the use of a post-dealloying thermal anneal in 5% $H_2/N_2$ at 400°C for 4 hrs (denoted un-annealed or annealed). ORR specific activities ($mA/cm^2$, at 900 mV in 50 $cm^2$ MEAs with 0.1 $mg/cm^2$ Pt loading[36] were measured for each catalyst. They were characterized structurally by HAADF ((high-angular annular dark field))/EELS (electron energy loss spectroscopy),[37] Pt $L_3$ and Ni K-edge EXAFS, Pt $L_3$ edge XANES (provided in Supplemental Figure S1–8; see the Supplemental Material link in the online version of this article), as well as Ni K μ XANES with full structural results to be reported elsewhere.[38] In general the particles are well formed 5–7 nm single core-shell particles (i.e. with a $PtNi_x$ core and a ~0.6 nm thick Pt shell).

### MEA tests

The MEAs were fabricated by a standard catalyst-coated membrane (CCM) method via draw down with a Meyer rod and subsequent decal transfer. This information is described

more fully elsewhere.[39] The above-prepared 50 cm$^2$ MEAs were tested for their cathode ORR kinetic activities under $H_2/O_2$ (anode/cathode); $H_2/O_2$ stoichiometries of 2.0 and 9.5, 100% relative humidity, cell temperature of 80°C, and at a back pressure of 150 kPa$_{abs}$. In voltage cycling tests, 200 sccm $H_2$ into anode and 50 sccm $N_2$ into cathode were admitted at 150 kPa$_{abs}$. The cell voltage was swept at 50 mV · s$^{-1}$ between 0.6 and 1.0 V (RHE) in a triangular profile for up to 30,000 cycles. The MEAs were subjected to the cathode catalytic activity ($H_2/O_2$) and the $H_2$/air performance tests after 200, 10,000, and 30,000 voltage cycles. The data collection procedures and conditions, specifically the ORR and ECSA measurements,[40] were performed according to the guidelines set by the USCAR Fuel Cell Tech Team (http://www.uscar.org/guest/view_team.php?teams_id=17). The mass and specific activities are summarized in Ref. 40 (page 9). A symbol translation table is provided in Supplemental Table S1 as the catalyst symbols adopted in Ref. 40 (page 7) are different from those used here (Table I).

### Electrode preparation and XAFS data collection

The electrode inks for the EXAFS electrodes were composed of 1:1 (wt%) 18.2 MΩ purity deionized water (Millipore) and 2-propanol (HPLC-grade, Aldrich), a 5 wt% Nafion solution (Aldrich), and the catalyst powder. The composition was chosen to give a final electrode with a dry Nafion loading of 5 wt%. The ink was hand-painted onto a Zoltek carbon cloth and dried for 15 minutes in a 65°C vacuum oven between coats. The final Pt and Ni geometric loadings were chosen to give ~0.05 edge heights at the Pt L$_3$ and Ni K edges, respectively. All data were collected in the fluorescence mode at beamline X3B at the National Synchrotron Light Source, Brookhaven National Lab. All of the experimental data were collected in conjunction with the appropriate reference foils to aid in energy alignment and normalization. A flow-through cell with continuously pumped 0.1M $HClO_4$ (GFS Chemicals) was constantly sparged with either argon (nitrogen) or oxygen gases (both high-purity). A high-purity, multiply-wound Au wire (+99.95%, Alfa Aesar) was used as the counter electrode, and a sealed saturated Ag/AgCl electrode (measured −0.283 V vs. reversible hydrogen electrode, RHE) served as the reference electrode. Potentiostatic control was maintained with an Autolab PGSTAT302N potentiostat/galvanostat (MetroOhm/ Brinkmann). The voltage cycling limits were 0.05 to 1.1 V vs. RHE. Data collection was performed at the chosen potentials held during anodic sweeps. Before each measurement, the cell was held for 5 minutes to reach a pseudo-steady-state, which is justified by the stable current density and the reproducibility of the data. The electrode was fully cycled following each potential hold in order to clean the electrocatalyst surfaces after each potential hold.

## Results and Discussion

### Catalysts structure and reactivity

Previously reported HAADF imaging data[40] for the as-prepared NAu (nitric acid un-annealed) catalysts dealloyed in an air vs. $N_2$ environment (i.e. resulting in ANAu vs $N_2$NAu dealloyed catalysts in Table I), showed the multi-core and porous structure of the ANAu catalysts vs. the more solid core in the $N_2$NAu case. The average NP size is around 5–7 nm, with the ANAu NPs having slightly larger size and greater size distribution.

Consistent with this, Fig. 1 showing the total coordination numbers (CN) of Pt, obtained from EXAFS analysis (provided in Supplemental Table S2), reveals that this difference in porosity remains even after 30 k electrochemical cycles. This cycling, done according to DOE (Department of Energy) standards[41] is utilized to perform an accelerated stress test. The $H_{upd}$ measured electrochemically active surface area (ESCA), as we move from the BOL (beginning of life), to 10 k and 30 k cycles (right to left) decreases because of growth in particle size and perhaps some removal of the under-coordinated sites at the particle corners and edges with cycling. But most importantly, the ANAu catalysts show a significantly lower CN at the same ECSA. This of course arises because of the multicore porous nature of the ANAu catalysts leaving Pt atoms uncoordinated at the edges/corners of the pores, throughout the cycling process. In contrast, the M-edge XAS data[38] utilizing Δμ analysis enables an in situ determination of when O atoms electrochemically adsorbed on the Pt surface penetrate the Pt skin to gain access to the underlying M atoms. These data show that the penetration potential of the different catalysts all merge to the same value after 30 k cycles and are close already at 10 k cycles. These results suggest that the thickness/ robustness of the Pt skins are similar after extensive cycling, but that the porosity existing in the core remains and this subtly alters the order existing in the Pt skin that affects the ORR.

Figure 2 shows a plot of Pt-Pt bond distance for the 16 catalysts as obtained from EXAFS analysis vs. the Ni/Pt ratio obtained from Energy Dispersive X-ray Spectroscopy (EDS) analysis after dealloying and cycling. The nearly linear slope confirms Vegard's law, and shows the nearly linear compression of the Pt-Pt distance with Ni/Pt ratio. The EXAFS data gives the average Pt-Pt distance throughout the entire cluster (core + skin), but the uniformly varying data in Fig. 3 strongly indicate that this general bulk compression also determines the strength of the Pt–O bond at the outer Pt skin. This is indicated by the systematic variation vs Ni/Pt ratio of the ORR specific activities (SA) in Fig. 3.

## Δμ XANES results

Δμ XANES data on the dealloyed NPs enable a direct measure of the $OH^*$, $OOH^*$ and $HOOH^*$ adsorbate intermediates on the Pt. The Δμ XANES data defined as, $\Delta\mu = \mu(A/Pt) - \mu(Pt)$ is surface sensitive because it involves the difference between the XAS absorption, when adsorbates are present, $\mu(A/Pt)$, vs when they are nearly absent $\mu(Pt)$, thus highlighting the small changes occurring due the adsorption. Small NPs are required for this measurement, as the ratio of surface atoms to all atoms are nearly negligible for the large polycrystals used by Stamenkovic et al.[13] Theoretical multiple scattering FEFF8[42] calculations enable identification of the different Δμ signatures for each adsorbate as reported previously in the literature.[12,43–50]

FEFF8 calculations on small $Pt_6$ model clusters to obtain theoretical signatures, $\Delta\mu = \mu(Ad/Pt_6) - \mu(Pt_6)$, have been shown to produce reliable Δμ signatures in excellent agreement with experiment for O, OH, CO (bridged and atop), H (3-fold vs atop), and other small adsorbates.[12,43–48] A $Pt_6$ cluster has been used often to model the experimental Pt clusters, as this highly asymmetrical cluster provides for all of the possible common binding sites[51] (fcc, hcp, bridged, and atop) and is asymmetrical so that it does not introduce any "surface resonances", which might arise from a more symmetric cluster,[52] and yet the

cluster is sufficiently large to account for the change in Pt-Pt scattering and new Pt-Ad scattering introduced by the adsorbate. Recently, calculations with increasingly bigger clusters ($Pt_6$, $Pt_{13}$ and $Pt_{25}$) were compared and found to give similar $\mu$ signatures,[53] and DFT calculations on slabs were shown to also give similar signatures as FEFF8 for O/Pt and CO/Pt.[54,55] These calculations show that the dominant contributions to $\mu$ are "local" to the Pt–O bond, and hence small clusters already give qualitative agreement with experiment, certainly sufficient to identify the binding site. Since the experimental data is an average over a wide array of particles sizes and shapes in a catalyst, any further attempt to improve on the model cluster to find more quantitative agreement between the experimental and theoretical signatures is deemed to be fruitless.

Pt $L_3$ XAS data were obtained in situ with the catalysts sparged in either $N_2$ or $O_2$. In $N_2$ any adsorbates must come from water activation, which generally occurs well above 0.54 V (rel. RHE), thus $\mu(0.54\ N_2)$ is taken as the reference as in our previous work. [43–48] Fig. 4 gives $\mu = \mu(V, O_2$ or $N_2) - \mu(0.54, N_2)$ for catalysts at several potentials showing how the $\mu$ signatures change with potential. Fig. 4 also gives FEEF8 signatures for $O^*$, $OH^*$, $OOH^*$, and $HOOH^*$ with adsorbate orientations as shown, and binding in the atop Pt sites. The position of the peak around 30–45 eV directly reflects the Pt–O bond distance reminiscent of EXAFS, and these are indicated in the figure going as $O < OH < OOH$; i.e. consistent with O bond order conservation. The feature around 5–20 eV reflects the x atom bonded on the outer side of the O atom in Pt–O-x, either nothing, O, or O + H. The second O backscatters the photoelectron so it produces the feature at 10–20 eV, and the H alters the feature between 3–10 eV as shown by the shaded regions. Comparison with the experimental signatures strongly suggest that with $N_2$ sparging at 0.9 V we have $OH^*$ and at 1.15 V mostly $O^*$ as shown many times before.[46–48] With $O_2$ sparging, at 0.54 V better agreement is evident with $HOOH^*$, at 0.74 V better with $OOH^*$, and at 0.9 with $OH^*$ and at 1.0 V apparently reflecting $O^* + OH^*$.

The results above confirm a di-oxygen species on the surface orientated with axis oblique to the Pt surface in an atop site with $O_2$ sparging. This is consistent with theoretical calculations.[56] DFT calculations on a $OOH/Pt_3$ cluster indicate that $OOH^*$ prefers a Pt atop site with axis oblique to the surface,[57] with Pt–O = 2.0 Å and O–O = 1.4 Å[58] in reasonable agreement with that found by comparison of FEFF8 and experimental signatures, 2.4 and 1.4 when OOH is bound to a 3–5 nm Pt particle. Similar calculations suggest $HOOH^*$ would orient as illustrated.[56,58] Finally calculations indicate a weakly bonded $O_2^*$ (0.3–0.5 eV compared to $O^*$ at 3.3–3.7 eV) would bond in a bridged site or in an fcc hollow site (atop-hollow-bridge); i.e., nearly parallel not oblique to the surface,[59] and therefore would give a $\mu$ significantly different from $OOH_n$.

Fig. 5 shows the amplitude of the $\mu$ maximum around 0–5 eV-above the Pt $L_3$ edge for the N2SAu catalysts, as shown in Fig. 4 as a function of potential after either $N_2$ or $O_2$ sparging of the $HClO_4$ electrolyte at the 3 different stages of life (BOL, and after 10 and 30 k cycles). Note that in $N_2$ sparged electrolyte, the $OOH_n^*$ coverage is negligible as the $OH^*$ comes just from water activation. In $O_2$ sparged electrolyte, the dioxygen species compete with the $OH^*$ species, so (as highlighted by the yellow arrow), the $OH^*$ coverage is decreased compared to the $N_2$ sparged electrolyte. The relative $OH^*$ at 0.9 V and $OOH_n^*$ coverage at

0.7 V given in Fig. 5 are those indicated by the height of the arrows for BOL and 30 K, and similar results for the 10 K data. The different potentials (0.7 in $O_2$ or 0.9 V in $N_2$) for the $OOH_n^*$ and $OH^*$ coverages, respectively, allow for the best separation of adsorbate species, when one or the other dominates.

The significant adsorbed dioxygen species evident down to 0.54 V in Fig. 5 confirms the effectiveness of our flow through cell, which pumps $O_2$ saturated $HClO_4$ electrolyte constantly to the cathode. It has been shown previously,[12] using μ XANES in a full operating fuel cell, that at the $O_2$ diffusion limit the coverage of nearly all adsorbed dioxygen species goes to zero as expected. In the fuel cell this occurred at high current and low cell potential, around 0.2–0.4 V. Similarly, Erickson et al,[34] using a specially designed high oxygen flux cell containing a poly(dimethylsiloxane) membrane with high permeability toward oxygen, found that the diffusion limit fell below 0.2 V. This is in contrast to typical RDE plots which typically show the diffusion limit occurring already around 0.85 V because of the low solubility of $O_2$ in water.[60] The much lower potential at the diffusion limit in fuel cells occurs in part due to the much larger IR losses at high currents in fuel cells,[12] but mostly due to the higher $O_2$ concentrations occurring in a fuel cell. In an *in operando* PEM fuel cell, humidified $O_2$ is continually pumped to the cathode via the gas diffusion layer. The continuous flow through cell utilized in this work is apparently also providing sufficient $O_2$ concentrations to the cathode to well below 0.5 V.

Figure 6 collects the μ and reactivity data from all 16 catalysts and shows how the $OH^*$ and $OOH^*$ coverages change with Ni/Pt near 0.8 V. It also shows that the specific area (SA) ORR activity of the solid NPs is indeed about 1.5–1.8 higher than for the porous NPs. The SA peaks with a typical asymmetric volcano curve at a Ni/Pt ratio of 0.17 (a bit higher for the solid case) and above 0.27 the additional Ni appears to have little effect. These SA ORR activity curves can be regarded as the NP equivalent of the previous polycrystalline data reported by Stamenkovic et al.[13] showing the difference between leached PtM (Pt skeleton) and annealed PtM (Pt skin) with M consisting of Ti, V, Fe, Co, and Ni. Similar to Fig. 6, their data showed increased SA for the annealed skin, with the volcano maximum moving to larger d-band shift (decreased Pt–O bond strength). Collectively these data are all consistent, and suggest strongly that the 111 planes are uniquely active compared to the other more open planes and corners/edges. Indeed these authors suggest that the most active $Pt_3Ni$ (111) SC catalysts known to exists, falls qualitatively on these volcano curves, and is the most active because of the SC 111 planes.[13] What is it about the Pt atoms on the 111 planes that make them the most active?

The results below Ni/Pt = 0.2 show typical Sabatier catalytic behavior. On the strong Pt–O bonding side of the volcano (low Ni/Pt ratio), relatively fast dissociative $O_2$ adsorption occurs with the slower step being H addition to $OH^*$ enabling it to leave the surface. As the Pt–O bond weakens with increasing Ni/Pt, the $OH^*$ coverage decreases, and the $OOH^*$ coverage increases due to the increasing difficulty of breaking the di-oxygen bond. The cross-over in coverage occurs right at the volcano maximum. Eq. 1 showed the simple rate expression,[13,20,21] $i \propto \exp(- G_{act}/RT) (1-\theta_{tad})$. We show in Fig. 6 a quantity equal to $0.55-\mu_{OH}-\mu_{OOH}-\mu_{HOOH}$ representing the relative $1-\theta_{tad}$, and it peaks very near the volcano maximum for the porous NPs as expected for typical Sabatier bahvior. The ORR rate does

not fall dramatically beyond Ni/Pt = 0.2 however because now the OOH mechanism takes over going as exp(− $G_{act}$/RT) $\theta_{OOH}$. The difference in rate dependece (1−$\theta_{tad}$) vs $\theta_{OOH}$ for these two cases occurs because with the dissociative $O_2$ mechanism, a later H addition to OH$^*$ cleans off the surface and is the potential determining step (pds), but with the OOH mechanism the first H adddition to $O_2$ is the pds (i.e. now the pds and rds are the same or the pds even precedes the rds).[8]

A significant difference occurs for the solid NPs, indeed 1−θ shows a double peak behavior with a minimum at the SA volcano peak. This 1−θ minimum falls right where the OOH$^*$ coverage shows a narrow maximum, much narrower than for the porous NP case. This narrowing is believed to arise because on the solid NPs H addition to OOH$^*$ is apparently able to occur at a much faster rate, changing OOH$^*$ to HOOH$^*$, which is then able to dissociate the di-oxygen bond much more easily. As a result OOH$^*$ coverage decreases and some HOOH$^*$ begins to build up only after the Ni/Pt ratio goes above 0.35. Thus each of the 3 di-oxygen dissociation mechanisms dominates at some point in the case of the solid NPs. The rate going as exp(− $G_{act}$/RT) (1−$\theta_{tad}$) now gives two separated peaks, the first as the dissociative $O_2$ mechanism switches to OOH and the second as OOH switches to HOOH. Between these two peaks the rate goes as exp(− $G_{act}$/RT)$\theta_{OOH}$, when the OOH mechanism dominates. Summed together only one assymetric and broader ORR volcano is visible.

The in situ μ XANES results suggest that the OOH$^*$ coverage markedly decreases in magnitude on 111 planar sites, because of a much faster addition of H to form HOOH$^*$ that can then undergo faster dissociation due to the weaker di-oxygen bond. Therefore the critical aspect must be something involving the binding of OOH$^*$ on these sites; i.e. a surface structural effect involving the OOH$^*$ bonding on the 111 sites must occur, which does not occur on the edge/corners or 100 sites. Recent DFT calculations reported by the Mavrikakis group[61] for ORR on Cu, Pd, Pt, Ag, and Au (111) planes, and reasonable least squares interpolation in between, reveals this significant change in OOH$^*$ binding upon moving from Pt to Ag, as highlighted in Fig. 7. This rearrangement dramatically decreases the activation energy for H addition to OOH$^*$ producing a minimum between Pt and Ag, i.e. right where PtM NPs would fall. Fig. 7 shows that the most stable binding of OOH$^*$ shifts from a atop/bridged site (closest O in the atop site, OOH over a bridge site) on Pt, to a bridge/fcc site (closest O in a bridged site, OOH over the fcc site) on Ag, Au. In contrast, the most stable site for the HOOH$^*$ is the same on all the M (111) surfaces. Therefore H addition to OOH$^*$ proceeds relatively easily over Pt that does not involve a rearrangement, but requires a much higher activation energy over Ag because of the required rearrangement. The minimum falls in between (i.e. for PtNi) when the OOH$^*$ binds the weakest, but has not yet changed binding sites requiring the rearrangement. This explains the trend in enhancement factors reported by Wagner et al.[62] The enhancement factor of 111 sites over other facet sites (111/100 or 111/110) is .82 and 0.35 respectively for Pt, but 20 and 8.2 respectively for PtNi. The enhancement factor is larger for PtNi when the Pt–O binding is near the minimum in Fig. 7.

Figure 7 also reveals some other basic points. Note the general increase in activation energy, $E_a$, for bond breaking and decrease of $E_a$ for H addition with Pt–O binding energy (BE$_o$), but as the results show, this trend is not monotonic but contains the minimum because of the

OOH[*] site rearrangement. Note also the general decrease in $E_a$ for breaking the O bond as the number of H atoms increase, the addition of H weakening the O–O bond. Results for H addition to the aquioxyl species (HHOO[*]) is also shown because this path is feasible, and HHOO has a very low $E_a$ for bond breaking.[61]

In summary, lattice compression (d-band shift) weakens the Pt–O bonding on NPs causing the OOH mechanism to dominate the ORR beyond Ni/Pt = 0.2. The OOH[*] site binding rearrangement on the 111 faces falling at Pt–O bond strength between Pt and Ag; namely around PtM, provides for optimal facile H addition enabling faster ORR reduction. Solid NPs have a larger number of these 111 planar sites because Pt atoms near the pores in the porous NP's contain more non-coordinated edge sites. Perhaps even more important, if we think of the porous NPs consisting of a Pt "blanket" over multicores, then the compression effect on the Pt skin might be very uneven, and this would also reduce the extent of order or number of 111 planes significantly; i.e. the Pt skin or blanket may have "wrinkles" and defects because of the underlying porous core structure. In either case, it is clear that significant surface effects exists particularly for these dealloyed PtM core-shell NPs, because of the important OOH[*] lattice rearrangement occurring right at the optimal Pt–O bond strength.

## Supplementary Material

Refer to Web version on PubMed Central for supplementary material.

## Acknowledgments

## References

1. Strasser P, Koh S, Anniyev T, Greeley J, More K, Yu C, Liu Z, Kaya S, Nordlund D, Ogasawara H, Toney MF, Nilsson A. Nat Chem. 2010; 2:454. [PubMed: 20489713]

2. Gan L, Heggen M, O'Malley R, Theobald B, Strasser P. Nano Lett. 2013; 13:1131. [PubMed: 23360425]

3. Hasché F, Oezaslan M, Strasser P. ECS Trans. 2011; 41:1079.

4. Koh S, Strasser P. J Am Chem Soc. 2007; 129:12624. [PubMed: 17910452]

5. Yu Z, Zhang J, Liu Z, Ziegelbauer JM, Xin H, Dutta I, Muller DA, Wagner FT. J Phys Chem C. 2012; 116:19877.

6. Jia Q, Segre CU, Ramaker D, Caldwell K, Trahan M, Mukerjee S. Electrochim Acta. 2013; 88:604.

7. Norskov JK, Bligaard T, Rossmeisl J, Christensen CH. Nat Chem. 2009; 1:37. [PubMed: 21378799]

8. Koper MM. J Solid State Electrochem. 2013; 17:339.

9. Stephens IEL, Bondarenko AS, Gronbjerg U, Rossmeisl J, Chorkendorff I. Energ Environ Sci. 2012; 5:6744.

10. Vegard L. Zeitschrift für Physik. 1921; 5:17.

11. Denton AR, Ashcroft NW. Phys Rev A. 1991; 43:3161. [PubMed: 9905387]

12. Ramaker DE, Korovina A, Croze V, Melke J, Roth C. Phys Chem Chem Phys. 2014; 16:13645. [PubMed: 24664398]

13. Stamenkovic VR, Mun BS, Arenz M, Mayrhofer KJJ, Lucas CA, Wang G, Ross PN, Markovic NM. Nat Mater. 2007; 6:241. [PubMed: 17310139]

14. Stamenkovic VR, Fowler B, Mun BS, Wang G, Ross PN, Lucas CA, Markovi NM. Science. 2007; 315:493. [PubMed: 17218494]

15. Wagner FT, Gasteiger HA, Makharia R, Neyerlin KC, Thompson EL, Yan SG. ECS Trans. 2006; 3:19.

16. Shao M, Peles A, Shoemaker K. Nano Lett. 2011; 11:3714. [PubMed: 21806027]

17. Nesselberger M, Ashton S, Meier JC, Katsounaros I, Mayrhofer KJJ, Arenz M. J Am Chem Soc. 2011; 133:17428. [PubMed: 21950956]

18. Mukerjee S, McBreen J. J Electroanal Chem. 1998; 448:163.

19. Jia Q, Caldwell K, Ziegelbauer JM, Mukerjee S, Ramaker DE. 2014 to be published.

20. Tarasevich, ASMR.; Yeager, E. Comprehensive Treatise of Electrochemistry. Plenum Press; New York: 1983. p. 301

21. Uribe, F.; Wilson, MS.; ST; Gottesfeld, S. Proceedings of the Workshop on Structural Effects in Electrocatalysis and Oxygen Electrochemistry. Scherson, DTD.; Daroux, M.; Xing, X., editors. The Electrochemical Society; Pennington, NJ: 1992. p. 494PV 92–11

22. Rossmeisl J, Logadottir A, Nørskov JK. Chem Phys. 2005; 319:178.

23. Nørskov JK, Rossmeisl J, Logadottir A, Lindqvist L, Kitchin JR, Bligaard T, Jónsson H. J Phys Chem B. 2004; 108:17886.

24. Rossmeisl J, Qu ZW, Zhu H, Kroes GJ, Nørskov JK. J Electroanal Chem. 2007; 607:83.

25. Watanabe M, Wakisaka M, Yano H, Uchida H. ECS Trans. 2008; 16:199.

26. Bligaard T, Nørskov JK, Dahl S, Matthiesen J, Christensen CH, Sehested J. J Catal. 2004; 224:206.

27. Herron J, Jiao J, Hahn K, Peng G, Adzic R, Mavrikakis M. Electrocatalysis. 2012; 3:192.

28. Nilekar AU, Mavrikakis M. Surf Sci. 2008; 602:L89.

29. Zhang J, Vukmirovic MB, Xu Y, Mavrikakis M, Adzic RR. Angew Chem. 2005; 117:2170.

30. Rossmeisl J, Karlberg GS, Jaramillo T, Norskov JK. Farad Discuss. 2009; 140:337.

31. Kunimatsu K, Yoda T, Tryk DA, Uchida H, Watanabe M. Phys Chem Chem Phys. 2010; 12:621. [PubMed: 20066348]

32. Ayato Y, Kunimatsu K, Osawa M, Okada T. J Electrochem Soc. 2006; 153:A203.

33. Shao, M-h; Liu, P.; Adzic, RR. J Am Chem Soc. 2006; 128:7408. [PubMed: 16756272]

34. Erickson EM, Thorum MS, Vasi R, Marinkovi NS, Frenkel AI, Gewirth AA, Nuzzo RG. J Am Chem Soc. 2011; 134:197. [PubMed: 22188603]

35. Casalongue HS, Kaya S, Viswanathan V, Miller DJ, Friebel D, Hansen HA, Nørskov JK, Nilsson A, Ogasawara H. Nat Commun. 2013; 4:1.

36. Kongkanand, A.; Wagner, F. [accessed January 6, 2014 ] Annual Merit Review. US Department of Energy Hydrogen and Fuel Cells Program. 2013. http://www.hydrogen.energy.gov/pdfs/review13/fc087_kongkanand_2013_o.pdf

37. Han B, Carlton CE, Kongkanand A, Kukreja RS, Theobald BR, Gan L, O'Malley R, Strasser P, Wagner FT, Shao-Horn Y. Energ Environ Sci. 2014 (Accepted for publication).

38. Caldwell KM, Jia Q, Mukerjee S, Ziegelbauer JM, Kukreja R, Kongkanand A, Ramaker DE. 2014 In preparation.

39. Gasteiger HA, Kocha SS, Sompalli B, Wagner FT. Appl Catal B-Environ. 2005; 56:9.

40. Kongkanand, A.; Wagner, F. [accessed July 30, 2014 ] Annual Merit Review. US Department of Energy Hydrogen and Fuel Cells Program. 2014. http://www.hydrogen.energy.gov/pdfs/review14/fc087_kongkanand_2014_o.pdf

41. DOE. U. S. D. o. Energy. Report to Congress. United States Department of Energy; Washington, DC: 2009. Hydrogen and Fuel Cell Activities, Progress, and Plans; p. 43

42. Ankudinov AL, Ravel B, Rehr JJ, Conradson SD. Phys Rev B. 1998; 58:7565.

43. Teliska M, O'Grady WE, Ramaker DE. J Phys Chem B. 2004; 108:2333.

44. Teliska M, O'Grady WE, Ramaker DE. J Phys Chem B. 2005; 109:8076. [PubMed: 16851943]

45. Teliska M, Murthi VS, Mukerjee S, Ramaker DE. J Electrochem Soc. 2005; 152:A2159.

46. Scott FJ, Roth C, Ramaker DE. J Phys Chem C. 2007; 111:11403.

47. Roth C, Benker N, Buhrmester T, Mazurek M, Loster M, Fuess H, Koningsberger DC, Ramaker DE. J Am Chem Soc. 2005; 127:14607. [PubMed: 16231913]

48. Scott FJ, Mukerjee S, Ramaker DE. J Electrochem Soc. 2007; 154:A396.

49. Kongkanand A, Ziegelbauer JM. J Phys Chem C. 2012; 116:3684.

50. Jia Q, Ramaker DE, Ziegelbauer JM, Ramaswamy N, Halder A, Mukerjee S. J Phys Chem C. 2013; 117:4585.

51. Janin E, von Schenck ouml H, thelid M, Karlsson UO, Svensson M. Phys Rev B. 2000; 61:13144.

52. Ramaker DE, Koningsberger DC. Phys Rev Lett. 2002; 89:139701. [PubMed: 12225071]

53. Jia Q, Caldwell K, Ramaker DE, Ziegelbauer JM, Liu Z, Yu Z, Trahan M, Mukerjee S. J Phys Chem C. 2014; 118:20496.

54. Lei Y, Jelic J, Nitsche L, Meyer R, Miller J. Top Catal. 2011; 54:334.

55. Guo N, Fingland BR, Williams WD, Kispersky VF, Jelic J, Delgass WN, Ribeiro FH, Meyer RJ, Miller JT. Phys Chem Chem Phys. 2010; 12:5678. [PubMed: 20442915]

56. Ou L, Yang F, Liu Y, Chen S. J Phys Chem C. 2009; 113:20657.

57. Seminario JM, Agapito LA, Yan L, Balbuena PB. Chem Phys Lett. 2005; 410:275.

58. Keith JA, Jacob T. Angew Chem Int Ed. 2010; 49:9521.

59. Stipe BC, Rezaei MA, Ho W, Gao S, Persson M, Lundqvist BI. Phys Rev Lett. 1997; 78:4410.

60. Schmidt TJ, Gasteiger HA, Stäb GD, Urban PM, Kolb DM, Behm RJ. J Electrochem Soc. 1998; 145:2354.

61. Ford DC, Nilekar AU, Xu Y, Mavrikakis M. Surf Sci. 2010; 604:1565.

62. Wagner FT, Lakshmanan B, Mathias MF. J Phys Chem Lett. 2010; 1:2204.

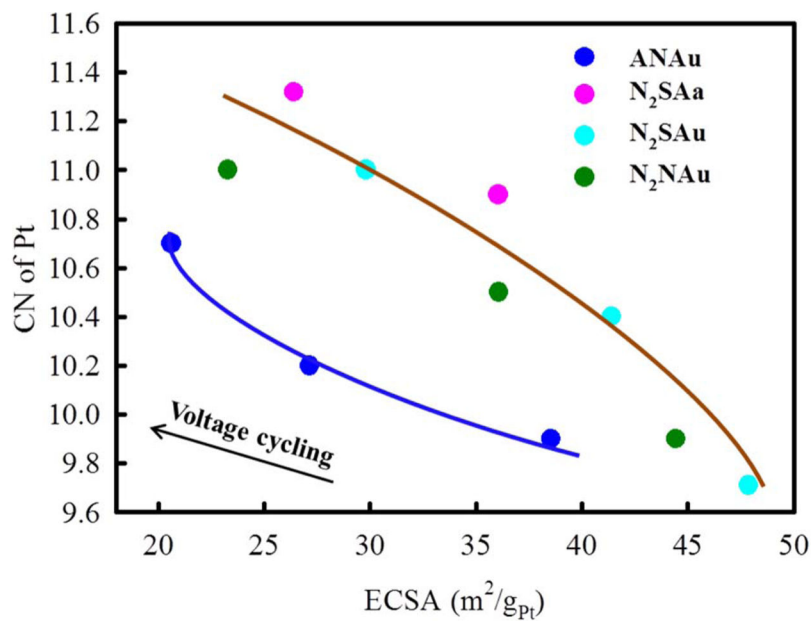**Figure 1.**
Pt-Pt coordination numbers obtained from in situ Pt $L_3$ EXAFS data as a function of $H_{upd}$ measured electrochemically active surface area (ECSA)[40] for the four catalysts indicated. Separate curves are drawn through the points for those catalysts prepared in an air (A) environment (blue) vs. those in an $N_2$ environment (red) distinguishing the more porous cores (ANAu) from the other more solid cores.
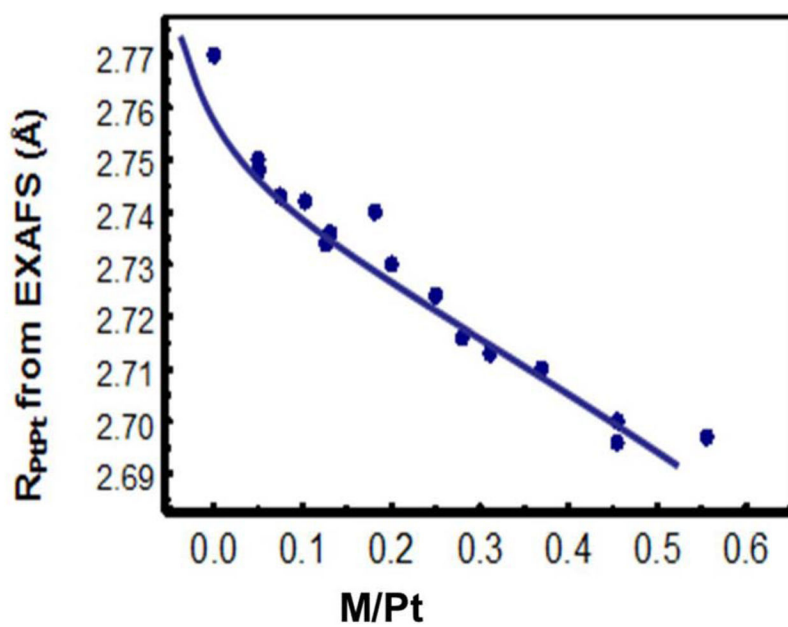
**Figure 2.**
Plot of Pt–Pt bond distance, $R_{PtPt}$ for 16 PtM catalysts and for Pt as obtained from EXAFS analysis vs. the M/Pt ratio obtained from Energy Dispersive X-ray Spectroscopy (EDS) analysis after dealloying and cycling.
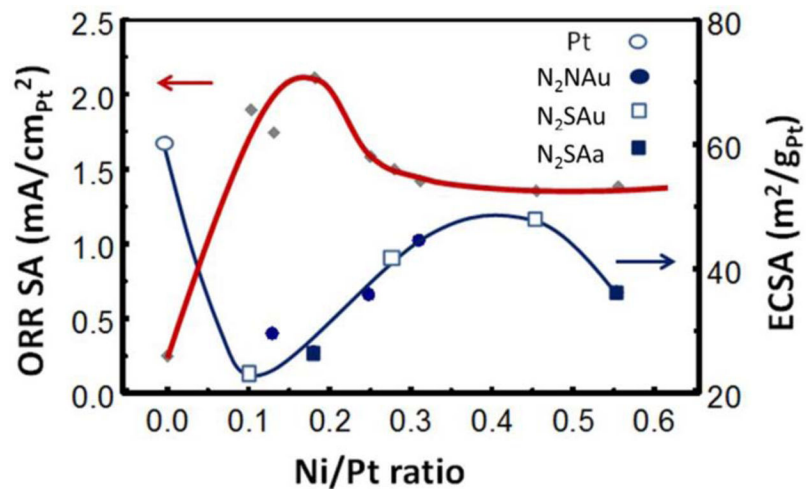
**Figure 3.**
ORR specific activity along with the electrochemical active surface area (ECSA)as measured with $H_{upd}$. The points on the ECSA curve indicate the catalysts with notation in the legend as in Table I. The BOL catalysts have the largest Ni/Pt ratio in each case, and ECSA decreases with cycling due to particle growth. Only BOL and 30 K results are available for the $N_2$SAa cataysts.
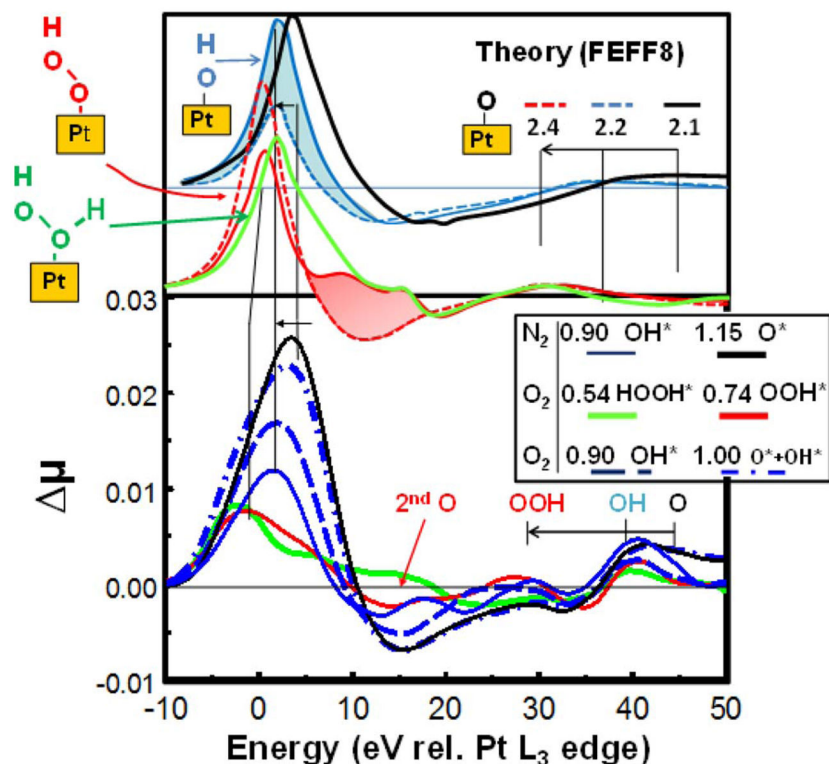
**Figure 4.**

$\mu = \mu(V, O_2 \text{ or } N_2 \text{ sparged}) - \mu(0.54, N_2 \text{ sparged})$ for the $N_2SAu$ catalyst after initial break-in (BOL) at the indicated potentials. Also indicated are FEFF8 results for the indicated adsorbates with Pt–O bond lengths as indicated in Å producing the shifts of the 30–45 eV peak (dashed lines show $\mu$ for just the O atom at the appropriate Pt–O bond length, solid for the full adsorbate such as OH* in blue and OOH* in red). The contribution from the second O in the OOH* is highlighted in red, that from the H in the OH in blue, as determined from the difference in $\mu$ with and without the second atom.
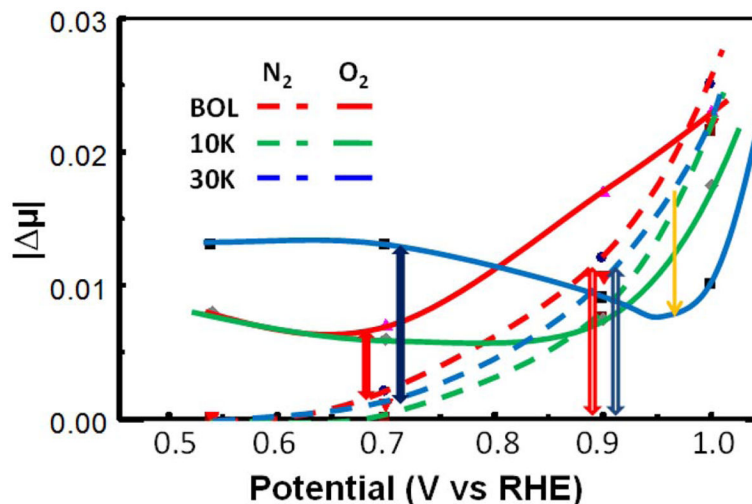
**Figure 5.**
Plot of | μ| magnitudes obtained from the peak heights around 0–5 eV above the Pt $L_3$ edge for the $N_2$SAu catalyst at 3 stages of life, BOL (200 cycles) and after 10 k and 30 k cycles(EOL), performed with DOE protocol, with $N_2$ or $O_2$–sparged electrolyte as indicated. The filled block arrows around 0.7 V indicate the relative coverage of $OOH^*$ at 700 mV (i.e. $OOH_n^*$ in the presence of $O_2$) and the open block arrows the coverage of $OH^*$ in $N_2$ (i.e. $OH^*$) near 900 mV. The yellow arrow indicates the drop in $OH^*$ around 0.95 V (vs. RHE) due to competition with $O_2^*$ for Pt sites.
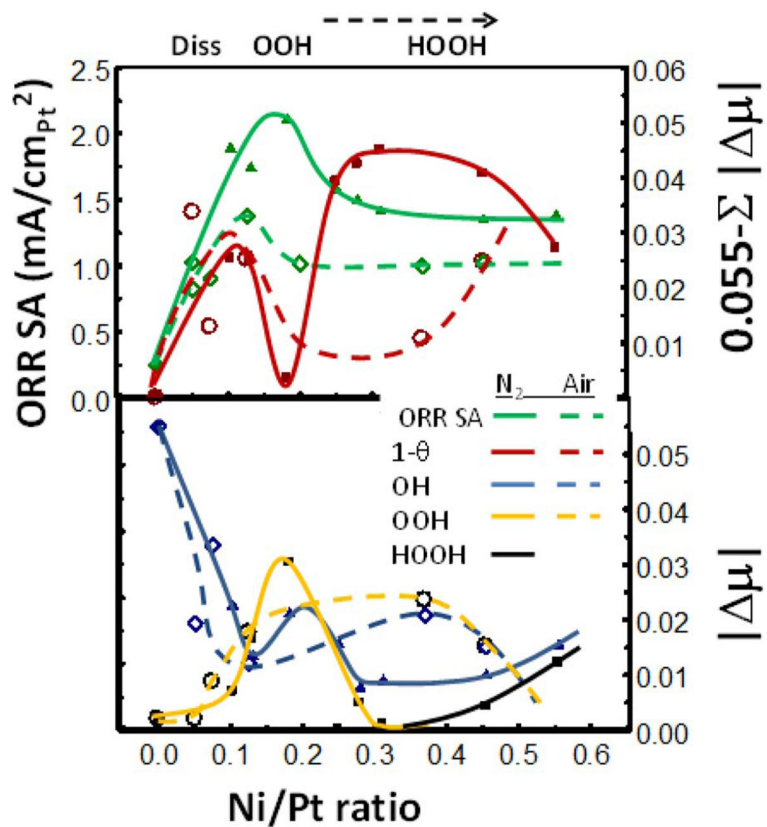
**Figure 6.**
Comparison of data for those catalysts de-alloyed in $N_2$ (solid) and those in air (porous). Top: Plot of ORR specific activity (SA) and $0.055 - \mu_{OH} - \mu_{OOH} - \mu_{HOOH}$ representing the number of empty Pt sites, $(1-\theta_{tad})$, during the ORR as a function of the Ni/Pt ratio. Bottom: Plot of $\mu_{OH}$ measured in $N_2$ sparged electrolyte at 0.9 V RHE and $\mu_{OOH}$ measured in $O_2$ sparged electrolyte during the ORR.
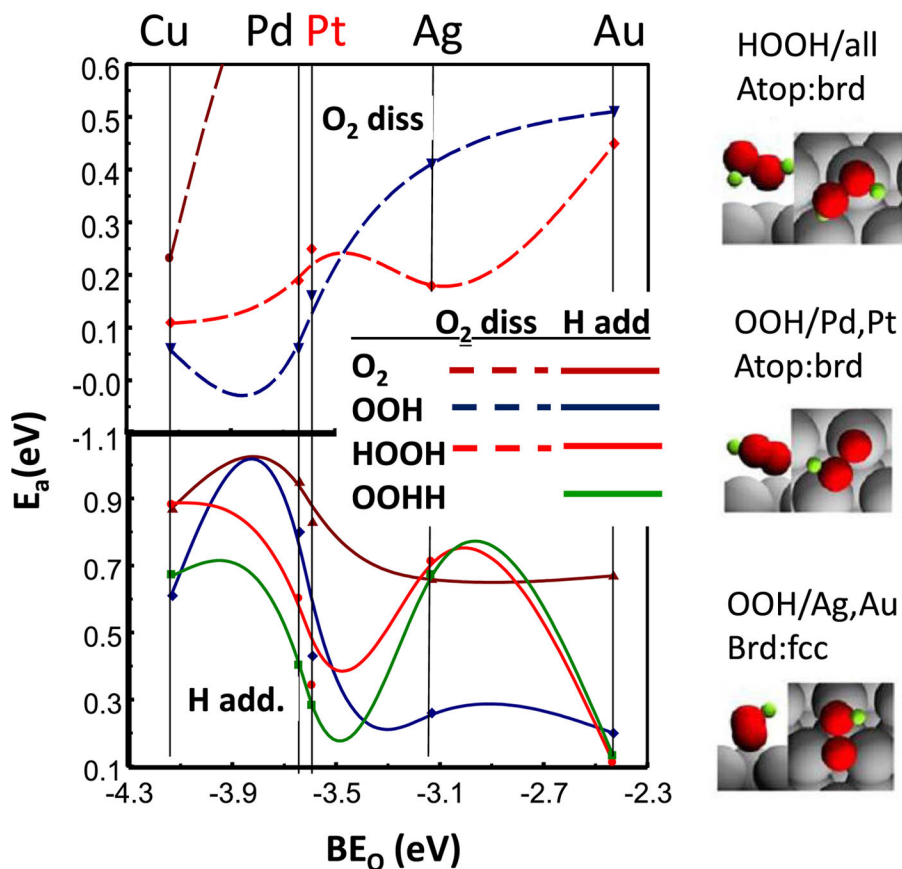
**Figure 7.**
Activation energies ($E_a$) obtained from DFT slab calculations for H addition (bottom) and O–O dissociation (top) as reported by Ford et al.[61] A least squares interpolation of the $E_a$'s is indicated between the M atoms. Schematic illustrations of the optimal binding sites of OOH and HOOH on Pt and Ag as estimated from the DFT calculations are indicated at the right. Adapted from Ref. 61 with permission from Elsevier Publishing, 2014.

**Table I**

Summary of catalysts studied.

| Catalyst symbol | Pre-cursor | Dealloying gaseous environment | De-alloying acid | Post annealing[1] | Life stages measured[2] | Morphology[3] |
|---|---|---|---|---|---|---|
| APtCo | PtCo | Air | $HNO_3$ | No | BOL | SC-NS |
| APtCo$_3$ | PtCo$_3$ | Air | $HNO_3$ | No | BOL,10 k,30 k | 50% MC-PS,50% SC-NS |
| ANAu | PtNi$_3$ | Air | $HNO_3$ | No | BOL,10 k,30 k | MC-PS |
| N$_2$NAu | PtNi$_3$ | N$_2$ | $HNO_3$ | No | BOL,10 k,30 k | SC-NS |
| N$_2$SAu | PtNi$_3$ | N$_2$ | $H_2SO_4$ | No | BOL,10 k,30 k | SC-NS |
| N$_2$SAa | PtNi$_3$ | N$_2$ | $H_2SO_4$ | Yes | BOL,10 k,30 k | SC-NS |

[1]Post annealed with a thermal treatment in 5% H2/N2 at 400°C for 4 hrs.

[2]XAS data at beginning of life; i.e. after around 200 cycles (BOL) or after 10,000 or 30,000 cycles (EOL) following DOE protocol.

[3]Morphology description obtained from TEM data: either multi- or single core PtM$_X$ (MC or SC) with porous or non-porous Pt skin (PS or NS).[40]